JOURNAL OF THERMOPHYSICS AND HEAT TRANSFER
Vol. 15, No. 4, October–December 2001

Experimental and Computational Study of Infrared Emission from Underexpanded Rocket Exhaust Plumes

G. Avital,* Y. Cohen,* L. Gamss,† Y. Kanelbaum,* J. Macales,*
B.Trieman,* and S. Yaniv‡
Israel Military Industries, Ltd., 47100 Ramat Hasharon, Israel
M. Lev§ and J. Stricker¶
Technion—Israel Institute of Technology, 32000 Haifa, Israel
and
A. Sternlieb**
DDR&D/IMOD, 61909 Tel-Aviv, Israel

Underexpanded rocket exhaust plumes generated in a test-bed facility are studied experimentally. Infrared (IR) images of the plume have been obtained with an IR camera equipped with narrow bandpass filters. The spectral distribution of the IR emission has been measured with a spectroradiometer. Numerical simulations of the exhaust plume have been conducted. The gas-dynamic and thermodynamic properties of the flowfield were computed by the General Aerodynamic Simulation Program computational fluid-dynamic code. On the basis of the simulated flowfield, the IR radiation was numerically calculated by using a computer program INFRAD, which has been developed for this purpose. The program calculates the radiation transfer through the plume using the statistical narrowband model technique. It allows simulation of the IR plume images as well as the local and the space-integrated plume spectra. The simulated and experimental results agree well.

Nomenclature

d	=	diameter
M	=	Mach number
$molf$	=	mole fraction
P	=	pressure
T	=	temperature
X	=	plume axis coordinate
$\boldsymbol{X}$	=	general chemical species
Y	=	radial coordinate
γ	=	specific heat ratio
ρ	=	density

Subscripts

a	=	ambient
b	=	blackbody
e	=	nozzle exit
s	=	stagnation
th	=	nozzle throat

I. Introduction

ROCKET-EXHAUST plume technologies are used for detection and tracking of rockets, identifying plumes of unfriendly vehicles, and distinguishing their emission from background signals. All of these applications require quantitative understanding of plume thermodynamic and gasdynamic behavior, the knowledge of its optical characteristics, and the ability to predict them.[1,2]

The rocket-exhaust plume represents an interesting object for pure scientific research, where complicated structure of shocks, expansion waves, and shear layers occur. It exhibits a unique phenomenon of extremely high-velocity, high-temperature, and often two-phase flow, including chemical processes.

Because the supersonic plume environment involves very high dynamic loads and high temperatures, difficulties arise for intrusive investigation of the plumes in flight and test bench conditions. Development of radiation diagnostics of such environments is therefore required both for scientific and technological research.

There has been significant progress in the numerical modeling of plumes in recent years.[3–5] However, because of the complexity and the variety of plume phenomena a reliable complete prediction of plume characteristics, including radiative and spectral features, is still an active research subject. The problem of reliable modeling includes testing various computer analyses and their validation by comparison with experimental data.

The objective of the present work is to evaluate the ability of the applied numerical procedure to predict the infrared (IR) radiation features of exhaust plumes and to study the degree of the model limitations. Particularly, this intention includes validation of the radiation code INFRAD developed for this purpose.

The results of an experimental investigation of the IR characteristics of a test-bed rocket-motor-exhaust plume are compared with the computational results. Such a study gives a better understanding of the physical and chemical structure of the plume flowfield.

The research includes three parts:

1) An experimental exhaust plume was generated by a small ballistic evaluation motor. IR images of the plume were obtained and spectroradiometric measurements of the plume were performed.

2) The thermochemical data inside the motor were calculated by the NASA thermochemical code CET89 (Ref.6). This data was used as input to the General Aerodynamic Simulation Program (GASP),[7] by which the plume flow field was simulated. The temperature, pressure and velocity fields were obtained, as well as the molecular species distribution.

3) Based on the computational fluid dynamics (CFD) results, the IR spectra and the IR images of the plume were calculated, using the INFRAD program. The calculated results were compared with the experimental IR images and spectroradiometric measurements.

Received 18 December 2000; revision received 8 May 2001; accepted for publication 9 May 2001.

*Research Scientist, Rocket Department.
†Head of the Research Group, Rocket Department.
‡Research Scientist, Rocket Department. Member AIAA.
§Research Associate, Faculty of Aerospace Engineering.
¶Associate Professor, Faculty of Aerospace Engineering. Member AIAA.
**Research Coordinator, Research and Development Department.

II. Experimental Setup

A. Ballistic Evaluation Motor

A solid-propellant ballistic evaluation motor (BEM) was used to generate underexpanded exhaust plumes. The first version of the motor (BEM-1), shown in Fig. 1, consists of a metal canister, fuel body, nozzle, and an annular nozzle holder. The throat and the exit diameters are $d_{\text{th}} = 15$ mm and $d_e = 25$ mm, respectively. As is seen in the figure, the nozzle holder creates an obstruction for observing the plume close to the nozzle exit. A second motor (BEM-2) was later used, in which a new nozzle with an improved holder was designed. The expansion cone of the nozzle was elongated; the throat and exit diameters were the same as in BEM-1. This was achieved by reducing the cone expansion angle from 19 to 15 deg. The BEM-2 nozzle enables observation of the exit plume, adjacent to the nozzle exit, and allows for simplified boundary conditions for the numerical code.

The internal combustion conditions were aimed at providing a steady plume during the motor firing. The propellant grain was a case bonded cylinder. The ratio of the grain length to its outer diameter was chosen to create a neutral burning pressure during a burn-out time of about 3.6 s. To create a one-phase gaseous plume, the propellant ingredients were chosen as to not include metal additives. The propellant grains contained 87% ammonium perchlorate oxidizer, 13% hydroxy-terininated polybutadiene binder and nonmetallic additives. In another batch the grains also included 0.5% SiC in order to dampen any possible burning instabilities. As it turned out, no burning instabilities were observed irrespective of the presence of the SiC. Addition of the SiC caused higher burning rates, as shown in Fig. 2, where two pressure traces, measured inside the chamber, are presented. The curves with the shorter and longer burning times represent the measurements performed with and without the SiC additive, respectively. It can be seen that in both cases the pressure stays almost constant during the burning time.

The small amount of SiC did not influence the plume chemistry, as verified by the negligible amount of condensed species found in the plume.

The stagnation parameters obtained in the motor are listed in Table 1.

The motor performance and the thermodynamic parameters at the nozzle throat were computed by an in-house CFD code and by the NASA thermochemical code CET89. The values of pressure, density, temperature, and specific heat ratio are summarized in the Table 1. The calculated chemical composition is given in Table 2. Calculation of the physical conditions and the species concentrations at the nozzle exit were conducted by a one-dimensional code and repeated by a two-dimensional code. A good agreement between the two calculations was obtained (see Sec. III).

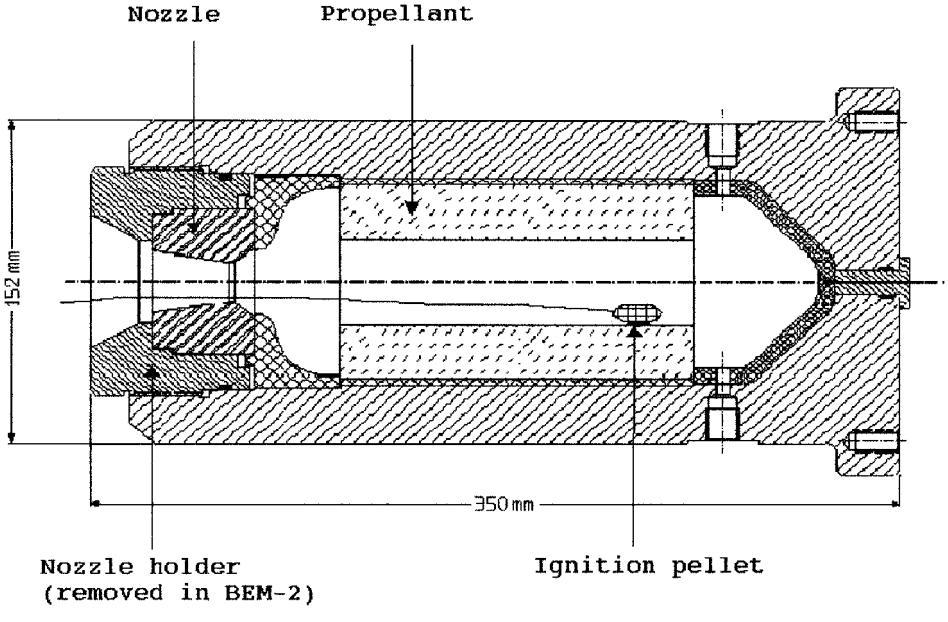

Fig. 1 Schematic of BEM-1.

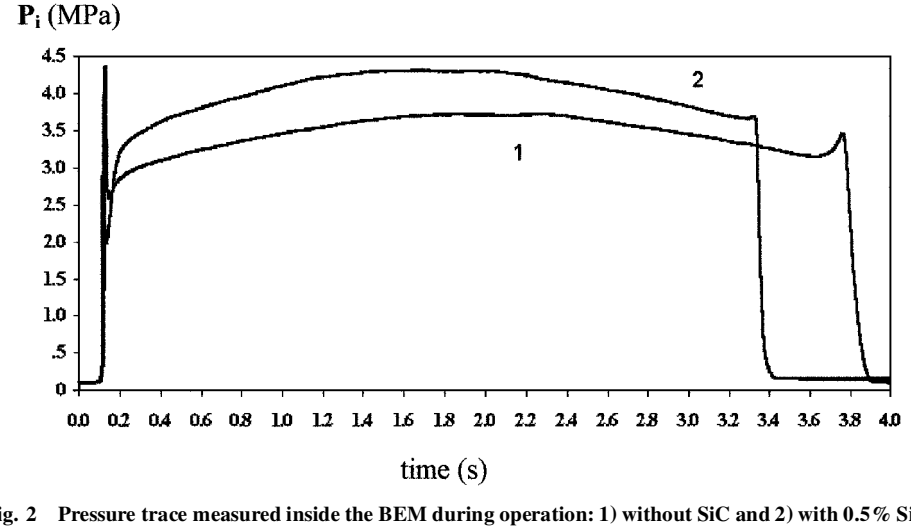

Fig. 2 Pressure trace measured inside the BEM during operation: 1) without SiC and 2) with 0.5% SiC.

Table 1 Pressure, temperature, specific heat ratio, and Mach number in the BEM

Location	Pressure, Pa	Temperature, K	γ	M
Stagnation	3.43×10^6	2930	1.16	0
Throat	2.24×10^6	2720	1.21	1
Exit	2.88×10^5	1960	1.30	2.35

Table 2 Species mole fraction in the BEM

Location	H_2O	CO_2	CO	N_2	H_2	OH	HCl
Throat	0.40	0.12	0.13	0.09	0.07	——	0.19
Exit	0.40	0.136	0.115	0.096	0.056	0.056	0.192

B. Radiation Measurements

The IR spectroradiometeric measurements were performed by using the SR-5000 spectroradiometer (CI Systems). This spectroradiometer covers the 1.4–14-μm wavelength region with the use of a circular variable filter wheel. The average spectral resolution is 0.02 μm ($\sim$20 cm^{-1} in wave numbers) in the 1.5–5.5 μm region, being studied. The uniformity of the sensitivity over the field of view (FOV) is typically within 5%. The measurements were carried out with FOV of 100 mrad and with scan rate of 10 scans/s.

The IR imaging was accomplished by using a RADIANCE-1 (Amber, Inc.) thermal imaging camera with 256×256 integrated indium antimonide focal plane array sensor. The calibrated camera operates as an IR imaging radiometer in the 3–5 μm spectral range. The spectral range can be narrowed by using of a replaceable narrow IR filter.

Both instruments were placed at a distance of 9.4 m from the plume. The calibration of the instruments was done by using a blackbody source. The calibration of the spectroradiometer was carried out with a blackbody temperature of $T_b = 1200$°C. The blackbody was located at the focus of a 12.7-cm-diam collimator, coincident with the plume position.

The RADIANCE-1 camera was also calibrated with the blackbody placed at the plume location. The calibration was performed by increasing the temperature of the blackbody from 800 to 1200°C by 100°C steps. The measured radiation of the blackbody aperture was corrected by subtraction of the background gray levels.

III. Exhaust Plume Simulations

A. Flowfield Simulations

Various gasdynamic discontinuities, such as Mach disk, barrel shocks, shear layers, shock-shock and shock-shear-layer interactions are present in the plume flow. To describe correctly the whole complex flow, the Navier–Stokes equations coupled with chemical kinetics must be applied. The gasdynamic computations have been performed using the GASP solver,[7] which is a general purpose CFD code for chemically reactive flows. Flow discontinuities can be captured by this code.

To obtain the gasdynamic and thermodynamic parameters at the nozzle exit, the internal nozzle flow was calculated by GASP for an axisymmetric flow model. Along the walls adiabatic, no-slip boundary conditions were used. The calculations begin at the nozzle throat, where the flow conditions, pressure, temperature, and specific heat ratio are those given in Sec. II. The thermodynamic parameters averaged over the exit cross section agree very well with those calculated by the one-dimensional code. The values obtained are given in Table 1.

A very low Mach number ($M = 0.2$) was assigned to the ambient freestream at the plane of the nozzle exit. This nonzero value, which differs from the experimental conditions, was assigned in order to improve the computational scheme for the compressible flow.[8]

To describe the external plume flow, the Reynolds-averaged Navier–Stokes equations coupled with the chemical kinetics are applied. The third-order Roe scheme with the min-mod limiter for the inviscid fluxes was used in the GASP code.

In the case of BEM-1, the plume flow adjacent to the nozzle exit is bounded by the nozzle holder walls. However, because the holder geometry is strongly overexpanded, the flow is expected to detach from its walls. For the flow within the holder walls zone, the Baldwin–Lomax turbulence model was applied.[9]

At the first stage of the research, the free plume flowfield was assumed to be laminar for both the BEM-1 and BEM-2 configurations. This assumption is valid only in the near-field region close to the jet exit, whereas downstream the flow becomes turbulent. The turbulence influences the mixing layer, which plays a significant role in the plume structure, in particular determining the length and the width of the plume. Neglecting the effects of turbulence reduces the accuracy of the solution mainly in the far field. Actually, to correctly calculate the plume over its total length the two-equation turbulence model (k–ε or k–ω model) is needed.[10] Subsequently the k–ω model was used for the BEM-2 configuration.

The far downstream boundary of the computation field was chosen to be 2 m downstream of the nozzle exit, where the characteristic subsonic conditions were defined. The same conditions are also used on the far radial boundaries. The singular axisymmetric conditions are used on the plume axis.

The primary chemical species in the exhaust gas are CO, CO_2, H_2O, H_2, OH, and HCl. The species mole fractions calculated by GASP at the exit plane of the nozzle are summarized in Table 2. Following Ref. 4, 10 chemical reactions between the plume species and the ambient atmospheric gases were considered:

$$\mathrm{OH + O \leftrightarrow H + O_2}, \qquad \mathrm{OH + H \leftrightarrow H_2 + O}$$

$$\mathrm{OH + OH \leftrightarrow H_2O + O}, \qquad \mathrm{OH + H_2 \leftrightarrow H_2O + H}$$

$$\mathrm{OH + CO \leftrightarrow CO_2 + H}, \qquad \mathrm{2H + \boldsymbol{X} \leftrightarrow H_2 + \boldsymbol{X}}$$

$$\mathrm{H + OH + \boldsymbol{X} \leftrightarrow H_2O + \boldsymbol{X}}, \qquad \mathrm{H + O + \boldsymbol{X} \leftrightarrow OH + \boldsymbol{X}}$$

$$\mathrm{2O + \boldsymbol{X} \leftrightarrow O_2 + \boldsymbol{X}}, \qquad \mathrm{CO + O + \boldsymbol{X} \leftrightarrow CO_2 + \boldsymbol{X}}$$

where $\boldsymbol{X}$ can be any one of the chemical species. The chemical reaction rates are included in the GASP database.

The HCl species was assumed as being nonreactive. It was shown in Ref. 11 that the conversion of the HCl into Cl occurs in a rocket plume afterburning region by the reaction:

$$\mathrm{HCl + OH \rightarrow Cl + H_2O}$$

However, it was shown for TITAN IV motors (15% of HCl mole fraction at the nozzle exit plane) that the degree of HCl dissociation is proportional to the plume altitude and to the distance from the nozzle exit.[11] It was found that at an altitude of 0.5 km about 90% of HCl molecules remained unreacted. For the present study with conditions of sea-level altitude and up to 2 m plume length, the dissociation of HCl can be considered negligible, and thus the HCl chemistry can be ignored. Indirect justification for this assumption is the agreement between the calculated and measured radiance at the HCl emission band (Sec. IV.C).

B. Infrared Radiation Calculations

For the numerical study of the spectral and radiative properties of the plume in the IR spectral range, the INFRAD program was developed. The program uses the narrow statistical band model technique to calculate the radiation transfer of nonuniform and nonisothermal media.[12] The code is based on Young's comprehensive analytical investigation of the various statistical band model techniques.[13] The "intuitive derivative approximation" (according to Young's terminology), which showed the best agreement with the experimental data of water vapor IR emission, was chosen in our code.[14]

The spectral resolution given by the code is determined by available band model parameters data and is typically 20 cm^{-1} in wave numbers.

The input to the program includes temperature, pressure, and species mole fraction fields, as calculated by GASP. The program

can simulate both the radiation emitted from a local plume volume and the integrated spectra over the whole plume length.

The molecular species and the temperature distributions, computed by the CFD code, were used in INFRAD to simulate the experimental images. The simulated IR images have been compared with the experimentally measured results.

IV. Results and Discussion

A. Results of the CFD Computations

Figure 3 presents calculated Mach contours in the near field of BEM-1. In this figure the characteristic structure of the plume flow pattern for the underexpanded nozzle $P_e/P_a \sim 3$ can be seen.[3,10,15] The Prandtl–Meyer expansion fan arises from the edge of the nozzle, tending to balance the exhaust gas pressure P_e and the ambient pressure P_a.[15,16] The cross section of the jet increases downstream of the nozzle exit, and the flow is accelerated.

The ensuing jet interface has a decreasing slope. The reflected waves from the ambient air are oblique shocks, where contraction and deceleration of the jet occurs. Their envelope line is a barrel shock. This barrel shock can be seen in the figure at the largest Mach value contour $M = 4.3$. The barrel shock collapses to a Mach disk. As is seen in the figure, a Mach reflected shock begins at the Mach disk. The reflected shock separates a domain, in which compressed, high-temperature flow exists. This domain strongly radiates and is known as a "diamond." Downstream of the Mach disk, there is a near-axial subsonic flow zone of the gas that has traversed the Mach disk. This zone has the highest pressure and temperature and, accordingly, is expected to exhibit the maximum radiance.

The cell pattern starts at the nozzle exit and terminates at the axial station, where the reflected shock intersects the plume interface. Hereafter, the expansion process begins again, similar to that at the nozzle exit, and the whole pattern repeats, resulting in appearance of several diamonds. Downstream, mixing of the plume with ambient air causes the wave pattern to fade out.

Figure 4 exhibits the calculated pressure along the flow axis of the laminar BEM-1 and turbulent BEM-2 plumes, where the location of the diamonds can be seen. Figure 4 shows a higher compression at the first diamond of the BEM-1 flow, as compared to the BEM-2 flow. It can also be seen that the damping of the pressure oscillations is faster for BEM-1 in spite of the turbulence assumed in the BEM-2 flow.

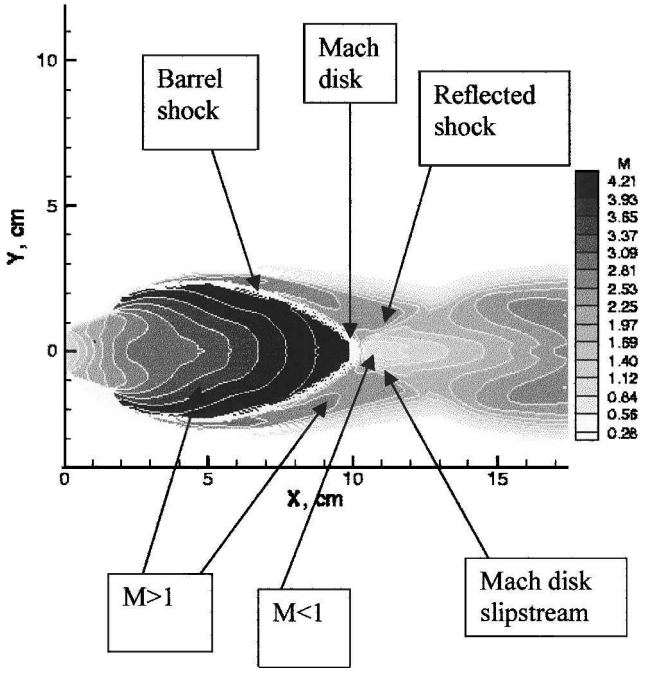

Fig. 3 Calculated Mach contours of BEM-1 plume.

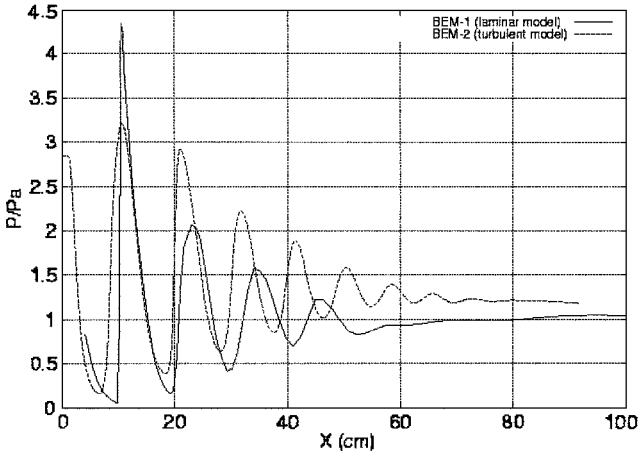

Fig. 4 Calculated pressure along the flow axis of the laminar BEM-1 and the turbulent BEM-2 plumes.

One of the reasons for the higher compression is that the nozzle expansion angle of BEM-1 is slightly larger than that of BEM-2. This causes a corresponding steeper turn of the diverging characteristics originating at the nozzle edge and, as a result, a steeper turn of the following converging characteristics. The high convergence of the flow leads to the higher compression observed in the BEM-1 plume. A second reason is the presence of the nozzle holder walls, causing the stronger reflection from the outer boundary. Calculations show that, although there is a Mach reflection in the plume of the BEM-1, a regular reflection takes place in the BEM-2 flow. The stronger compression in BEM-1 also affects the temperature field. Figures 5a and 5b show the calculated temperature fields in the near region of the laminar BEM-1 plume, where the weak effect of the turbulence can be expected, and for the BEM-2 turbulent plume model, respectively. The laminar model for the BEM-2 gives a different temperature field from the BEM-2 turbulent model for the same initial conditions. The maximum temperature in the first diamond of the laminar BEM-2 plume was about 350 K lower than in the laminar BEM-1 plume because of lower compression in BEM-2. For the turbulent model of BEM-2, the heat losses increase, and the temperature even in the first diamond is 300 K lower than in the laminar BEM-2 plume.

The CO_2 mole concentration in the BEM-2 turbulent plume is shown in Fig. 6 for later comparison with measured IR images, taken in the characteristic spectral range of CO_2 emission. It can be seen that the concentration of CO_2 varies by a factor of three over the diamonds and intermediate regions.

B. Plume Images

Typical experimental images of the BEM-1 and BEM-2 plumes are shown in Figs. 7a and 8a, respectively. The images shown were obtained sequentially in one motor firing. The time intervals between images are 0.5 s and 1 s for BEM-1 and BEM-2, respectively. The images were taken by the RADIANCE-1 camera with bandpass filters of 4.527–4.615 μm for the BEM-1 plume and 4.372–4.516 μm for the BEM-2 plume.

The BEM-2 images, shown in Fig. 8a, exhibit the known structure,[3] schematically illustrated in Fig. 8b (reproduced from Ref. 3.) The plume can be subdivided into three zones:

1) The first zone is the near field, ~30 cm from the nozzle, where the plume structure is determined solely by the pressure ratio between the exhaust gases and the ambient air. In this region the mixing process is confined to a thin layer.

2) A transitional region is the second zone, where the wave structure is smeared. The wave strengths dissipation can be seen, resulting from an interaction process between the plume and ambient air. The mixing layer penetrates to the plume axis.

3) The third zone is the far field, where wave processes has totally diminished and the flow becomes fully turbulent. This region is clearly seen to begin at a distance of ~60 cm from the nozzle exit.

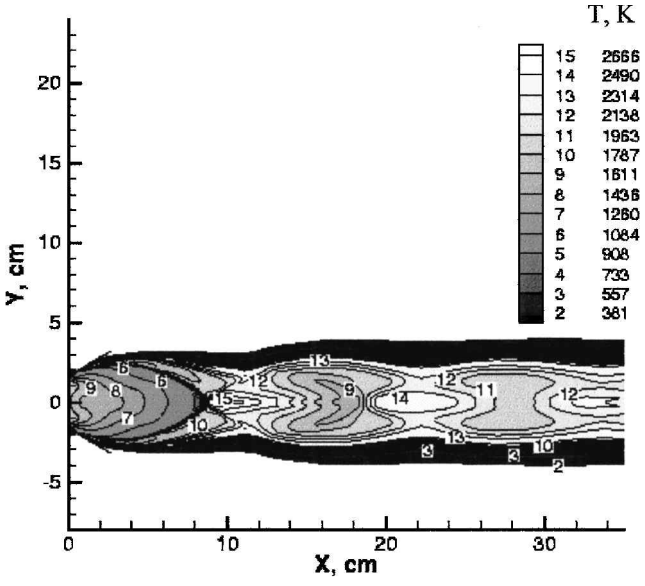

Fig. 5a Calculated temperature field for the laminar BEM-1 exhaust plume.

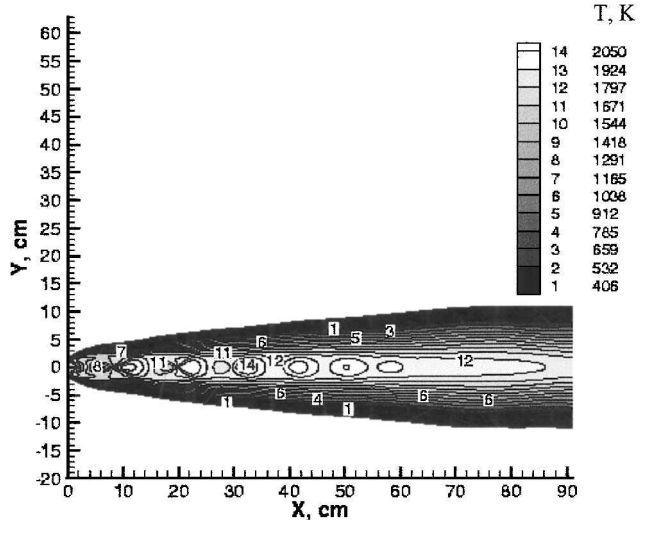

Fig. 5b Calculated temperature field for turbulent BEM-2 exhaust plume.

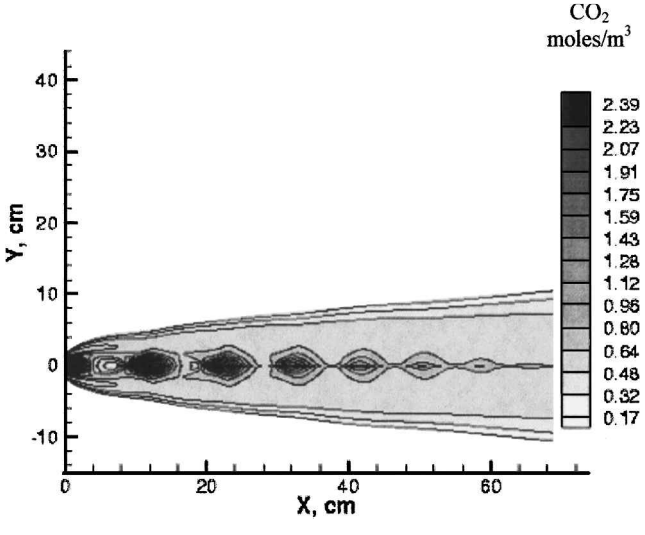

Fig. 6 Calculated CO_2 molar concentration for the BEM-2 turbulent plume.

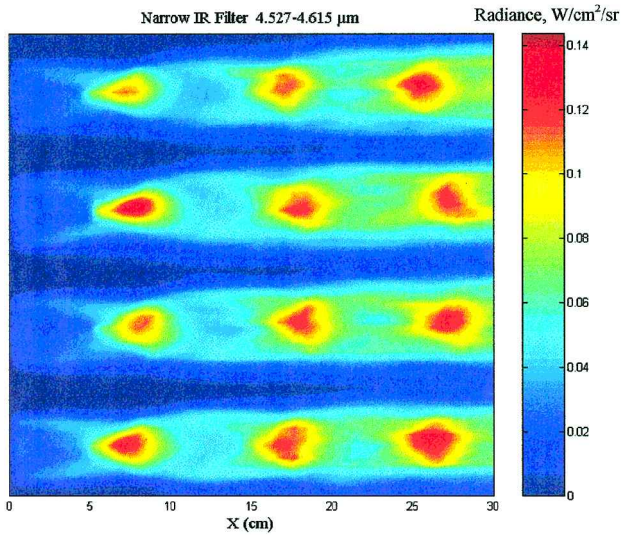

Fig. 7a Experimental IR images of BEM-1 plume obtained sequentially in one run. Time between images ~0.5 s. Bandpass filter 4.527–4.615 μm. $X = 0$ is at the nozzle holder exit plane.

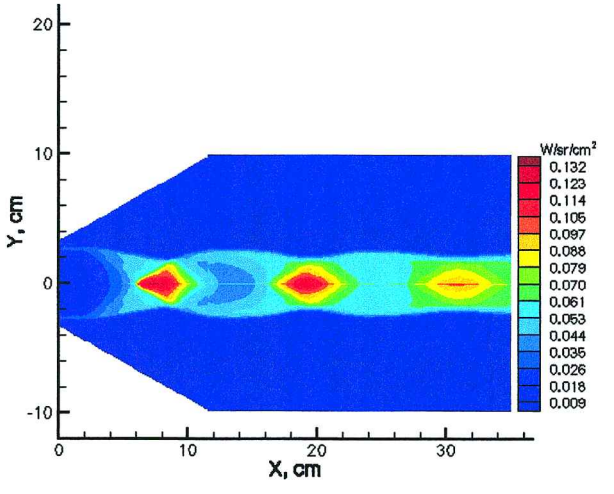

Fig. 7b Synthetic IR image of BEM-1 plume (laminar model). Bandpass filter 4.527–4.615μm. $X = 0$ is at the nozzle holder exit plane.

Figure 7a shows only the near field, ~30 cm in length, of the BEM-1 plume images. To be noted is that in Fig. 7a the coordinate origin $X = 0$ is at the nozzle holder exit plane, from which an observable plume starts, rather than at the nozzle exit as in Figs. 8a and 8c. As seen in the figure, the flow in the near field is mainly laminar, and, therefore, the laminar model, used for BEM-1 plume, gives satisfactory results for this flow region.

Both bandpass filters, used in the BEM-1 and BEM-2 experiments, fall within the characteristic radiation of the 4.3-μm fundamental molecular band of CO_2, with only a minor contribution of CO emission. This molecular band was chosen because it is known to be the strongest IR radiator among the characteristic plume species. The wider bandpass filter was used for BEM-2 plume to better capture the peak of the CO_2 emission.

As was already noted, the CFD calculations show a three-fold variation of the CO_2 concentration between the diamond and intermediate regions (Fig. 6). The temperature in the diamonds is about 25% higher than in the intermediate regions. However, the diamonds are only 2.3 times brighter than the region between them (Figs. 7a and 8a). This indicates that the outer plume layer smoothes the radiative contrast of plume core.

The plume images, shown in Figs. 7a and 8a, allow the identification of the reflected shocks and the measurement of their angles, as well as distances between sequential Mach disks. Comparison

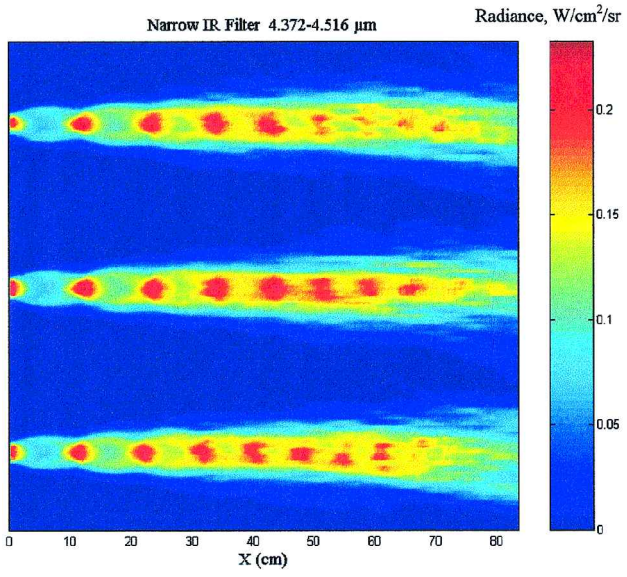

Fig. 8a Experimental IR images of BEM-2 plume, obtained sequentially in one run with the 1-s interval between scans. Bandpass filter 4.372–4.516 μm. $X = 0$ is at the nozzle exit plane.

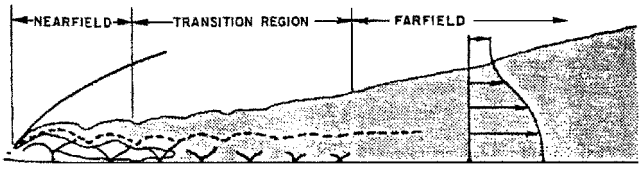

Fig. 8b Structural features of plume near field, transition region, and far field (reprinted from Ref. 3).

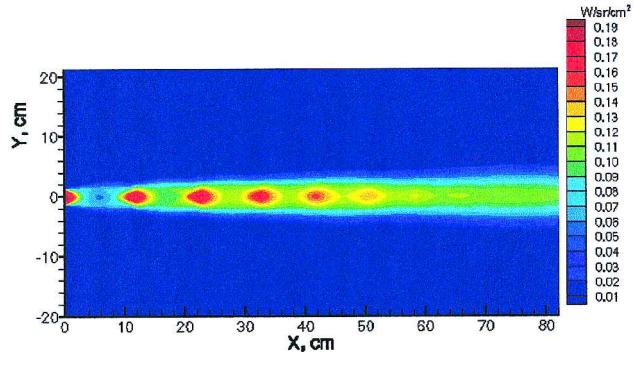

Fig. 8c Synthetic IR image of BEM-2 plume (turbulent model). Bandpass filter 4.372–4.516 μm. $X = 0$ is at the nozzle exit plane.

between these images and the simulated ones, illustrated in Figs. 7b and 8b, shows good agreement, in spite of the complex two-stage (fluid dynamic and radiative) simulation procedure.

For example, for BEM-1 the measured angle between the first reflected wave and plume axis is 25 deg with 15% accuracy (Fig. 7a). This is in agreement with the angle of 30 deg measured on the synthetic images for BEM-1 (Fig. 7b). The measured distance from the nozzle holder exit to the first Mach disk is 5.5 ± 0.3 cm (8.1 ± 0.3 cm from the nozzle exit), whereas the calculated distance is 5.7 cm, which lies within the experimental dispersion.

For BEM-2 the measured distance of first Mach disk from the nozzle exit is 9.1 ± 0.3 cm (Fig. 8a). The differences between these measured values for the BEM-1 and BEM-2 plumes provide experimental evidence for the steeper first reflection in the BEM-1 plume compared with BEM-2 plume, as was discussed in Sec. IV.A. The calculated distance from the nozzle exit to the first Mach disk is 9.3 cm, which also lies within the experimental dispersion.

The measured distance between the first and the second Mach disks is 10 cm for BEM-1 and 11.6 cm for BEM-2 within the same

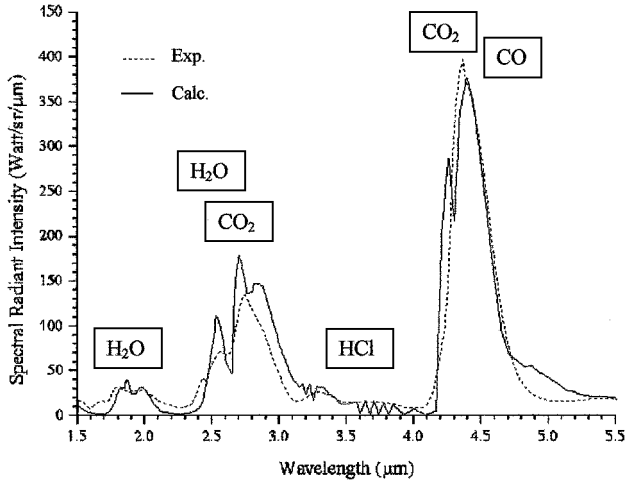

Fig. 9 Measured and calculated IR spectra of the BEM-2 plume emission, integrated over 1 m of plume length (turbulent model).

3% accuracy (Figs. 7a and 8a). The calculated laminar models overestimate these values both for BEM-1 and BEM-2 plumes. The laminar model for BEM-1 gives 10.8 cm, which is within 8% of accuracy. The laminar model for BEM-2 overestimates this value by 10%, namely giving the value of 11.3 cm. The result obtained with the turbulent model (BEM-2) is 11.3 cm, which is within 3% of accuracy.

As was expected, the best agreement, 20% of accuracy, between the calculated laminar plume structure and experiment is obtained in the near field, to a downstream distance of about 15 nozzle exit diameters for BEM-1 and to 10 nozzle exit diameters for BEM-2. The discrepancy between the laminar model calculations and experimental images progressively increases with the distance from the nozzle. The turbulent pattern is clearly seen in the experimental images, the distance between diamonds becomes shorter, and finally the diamonds disappear. The simulated laminar pattern for BEM-2 shows that the periodical structure remains at significantly longer distances in contrast with observations. The turbulent model allows extending the agreement to the far field (Fig. 8a). The decay of the wave structure at 25 exit diameters downstream from the nozzle exit is obtained on the simulated images, which agree with the experimental observation, as well as the number and shape of the legible diamonds.

The agreement between the measured and calculated radiance is within 5–10% for the turbulent model.

C. Plume Spectrum

Spectral measurements in real rocket flight conditions are usually performed by collecting the integrated emission from the whole plume length. Although these measurements do not give detailed information on the plume structure, they can be used for plume characterization. The plume spectrum of this kind is known in literature as the plume "signature."[2]

A typical experimental plume spectrum, integrated over 1 m of BEM-2 plume length, is shown in Fig. 9. Sequential scans of the plume spectrum during one firing give almost identical results indicating high plume stability. Also in Fig. 9 the synthetic spectrum, integrated over the same plume length, is shown. The spectrum was calculated using the results of the turbulent model. The locations of the characteristic bands of the molecular species are marked on the figure.

Comparison between experimental and calculated spectra reveals good agreement for the turbulent model results, shown in the figure. The laminar model results (not shown in the figure) overestimate the experimental results by a factor of ~1.4 over almost all of the spectral range. This result can be explained by the effect of turbulence, which leads to a more intense mixing of the hot exhaust gas with the cold ambient air, causing increased heat exchange. Thus for the laminar model overestimation of the temperature values appears mainly in the transitional and far-field regions.

An overshoot of the predicted spectra is observed at the 2.7-μm H_2O band by a factor of about 1.5; its origin is not clear yet.

V. Summary

The comparison between the numerically simulated BEM exhaust plumes and the experimentally measured plumes shows good agreement. The numerical simulations quite accurately describe the basic gas dynamic, thermodynamic, and radiative characteristics of the plume. Comparison of the detailed features, such as plume spatial structure and spectral radiative intensity, shows that an accuracy of better than 10% can be achieved by the calculations.

For the near field of the plume, a laminar model can be applied. At a distance of about 20 nozzle exit radii, the effect of turbulence causes a significant departure between the mathematical model and experimental measurements. Application of the $k-\omega$ two-equation turbulence model allows good agreement to be extended up to 50 nozzle exit radii.

Images of the plume were obtained using narrowband filter within the CO_2 fundamental vibrational band. These images show the flow structure of the plume. The measured spatially integrated spectra agree very well with the calculated spectra except for the discrepancy in the H_2O 2.7-μm band.

Acknowledgments

The authors wish to thank A. Devir and A. Lessin of Institute of Advanced Research and Development, Haifa, Israel, for useful and encouraging discussions during the work.

References

[1]Sutton, G. P., *Rocket Propulsion Elements*, Wiley, New York, 1992, pp. 549–563.

[2]JANNAF Handbook, *Rocket Exhaust Plume Technology*, CPIA publ. 263, Johns Hopkins Univ., Laurel, MD, 1980, Chap. 3.

[3]Dash, S. M., and Sinha, N., "Exhaust Plumes and Their Interaction with Missile Airframes: A New Viewpoint," *Tactical Missile Aerodynamics*, edited by M. R. Mendenhall, Vol. 142, Progress in Astronautics and Aeronautics, AIAA, Washington, DC, 1992, pp. 649–756.

[4]Hong, J. S., Levin, D. A., Collins, R. J., Emery, J., and Tietjen, A., "Comparison of Atlas Ground Based Plume Imagery with Chemically Reacting Flow Solutions," AIAA Paper 97-2537, June 1997.

[5]Vitkin, E. I., Karelin, V. G., Kirillov, A. A., Suprun, A. S., and Khadyka, Ju. V., "A Physico-Mathematical Model of Rocket Exhaust Plumes," *International Journal of Heat and Mass Transfer*, Vol. 40, No. 3, 1997, pp. 1227–1240.

[6]Gordon, S., and McBride, B. J., "Computing Thermodynamic and Transport Properties," NASA Tech Briefs, Vol. 17, Issue 7, July 1993.

[7]GASPex, Ver. 3, User's Manual, AeroSoft, Inc., Blacksburg, VA, 1997.

[8]Turkel, E., "Review of Preconditioning Methods for Fluid Dynamics," *Applied Numerical Mathematics*, Vol. 43, No. 12, 1993, pp. 257–264.

[9]Baldwin, B. S., and Lomax, H., "Thin Layer Approximation and Algebraic Model for Separated Turbulence Flows," AIAA Paper 78-257, Jan. 1978.

[10]Wilcox, D. C., *Turbulence Modeling for CFD*, 2nd ed., DCW Industries, La Canada, CA, 1998, pp. 83–92.

[11]Zittel, P. F., "Computer Model Prediction of the Local Effect of Large, Solid Fuel Rocket Motors on Stratospheric Ozone," Aerospace Corp., No. TR-94(4231)-9, El Segundo, CA, Sept. 1994.

[12]Ludwig, C. B., Malkmus, W., Reardon, J. E., and Thomson, J. A. L., "Handbook of Infrared Radiation from Combustion Gases," NASA SP-3080, 1973.

[13]Young, S. J., "Nonisothermal Band Model Theory," *Journal of Quantitative Spectroscopy and Radiative Transfer*, Vol. 18, No. 1, 1977, pp. 1–28.

[14]Young, S. J., "Evaluation of Nonisothermal Band Model for H_2O," *Journal of Quantitative Spectroscopy and Radiative Transfer*, Vol. 18, No. 1, 1977, pp. 29–35.

[15]Abramovich, G. N., *The Theory of Turbulent Jets*, Massachusetts Inst. of Technology Press, Cambridge, MA, 1963, pp. 335–344.

[16]Shapiro, A., *The Dynamics and Thermodynamics of Compressible Fluid Flow*, Wiley, New York, 1953, pp. 479–502.